

<https://doi.org/10.1038/s40494-025-02046-6>

Petrophysical and mechanical characterization of sandstones from different grottoes in China

Check for updates

Xiuwei Guo^{1,2}, Yue Zhang^{2,3,4}✉, Rongrong Hao^{1,2}, Ruoyu Zhang^{1,2}, Yuan Cheng^{2,5} & Jizhong Huang^{2,5}✉

Sandstone grottoes, characterized by their magnificent carvings and massive quantity, are of significant value to humanity and constitute an integral part of China's cultural heritage. Their physical and mechanical properties depend on composition, texture, and weathering degree. This study analyzes four sandstone grottoes, i.e., Yungang Grottoes (YG), Tianlongshan Grottoes (TLS), Leshan Giant Buddha (LS), and Dazu Rock Carvings (DZ), using ICP-OES, XRD, SEM, MIP, petrography, and mechanical tests. Results show that mechanical properties are correlated with porosity, pore structure, density, and cementation. Pore structure influence strength, with unimodal pore distributions exhibiting greater strength than multimodal ones. Petrographic analysis confirmed that mechanical properties are primarily controlled by grain contact and cementation. Among quantitative petrographic indices evaluated, GVCM index demonstrated particular reliability in predicting sandstone strength. These findings highlight the importance of petrographic features in assessing sandstone stability, aiding conservation efforts for these heritage sites.

China is renowned for its unique grottoes, which are scattered across the vast expanse of the country. Among them, approximately 80% grottoes in China were carved on sandstone strata. The choice of sandstone as the foundational substrate for the grottoes reflects a careful consideration of both geological availability (covering 15% of the continent surface¹) and material characteristics. As weakly-bonded sedimentary rocks composed of sand-sized grains (0.063–2 mm) and cement, sandstones offered workable yet durable material². These two reasons made sandstone grottoes a significant part in the architectural heritage of numerous ancient civilizations around the world. However, after years of weathering, these precious sandstone heritages have suffered from severe and complicated deterioration, leading significant challenges for their preservation. To represent the diverse regions and environmental conditions of sandstone grottoes in China, four significant sites were selected based on their historical importance and geographical representativeness. The Yungang Grottoes and Tianlongshan Grottoes were chosen to represent the northern China and semi-arid climate, while the Dazu Rock Carvings and Leshan Giant Buddha were selected as characteristic examples from southwestern China's subtropical region. Notably, three of these sites—the Yungang Grottoes, Dazu Rock

Carvings, and Leshan Giant Buddha—have been designated as UNESCO World Heritage Sites.

In response to these challenges, researchers and conservators specialized in various fields have spent years working on the protection and conservation of grottoes in China. Over the years, protection and conservation projects conducted across the country, solving pressing situations, especially structural problems^{3–5}. To develop effective conservation strategies, a deeper understanding of the material properties of sandstone is essential, as these properties directly influence the strength and durability of the grottoes. The strength and durability of sandstones are dependent upon the petrographic and petrophysical properties^{6–8}. All characteristics are coupled anyhow with one another directly or indirectly. Slight variations in either composition or pore geometry can result in substantial differences in strength and durability. Hence, each small progress is a step towards the objective to explain behavior of a stone by its physical-technical data, to forge a link between a porous material's structure and its intrinsic characteristics⁹.

Previous studies have extensively investigated the relationships between various physical/mechanical properties of sandstones^{10,11}, including hardness^{12,13}, ultrasonic velocity¹⁴, and texture⁷, etc. The mechanical

¹School of Mechanics and Engineering Science, Shanghai University, Shanghai, China. ²Institute for the Conservation of Cultural Heritage, School of Cultural Heritage and Information Management, Shanghai University, Shanghai, China. ³China-Portugal Belt and Road Joint Laboratory on Cultural Heritage Conservation Science, Suzhou, China. ⁴International Cooperative Joint Laboratory of Cultural Heritage Conservation Science supported by the Belt and Road Initiative, Suzhou, China. ⁵Key Laboratory of Silicate Cultural Relics Conservation (Shanghai University), Ministry of Education, Shanghai, China.

✉ e-mail: 2019zhangy@shu.edu.cn; hjizhong@163.com

behavior appears significantly influenced by petrographic characteristics^{15–17}, particularly grain-related properties. Research indicates that sandstones with higher quartz content¹⁵, greater angular grain content¹⁸, increased packing density/proximity¹⁹, and better grain contact²⁰ generally exhibit enhanced strength. Grain sorting plays a crucial role, as poorly-sorted sandstones typically demonstrate superior mechanical strength due to improved grain-to-grain contact²¹. Finer sand particles also increase grain-to-grain contact by filling voids between larger grains²². However, the relationship between mineral composition and strength remains complex - while some studies report positive quartz content-UCS correlations^{15,23}, others observe negative correlations²⁰, suggesting no universal trend. These discrepancies likely arise from regional variations in diagenesis and weathering processes that modify original grain characteristics.

Despite the numerous studies focused on sandstones' physical and mechanical characteristics, the petrophysical properties of important Chinese grotto sandstones remain poorly understood. Hence, in order to understand weathering mechanism of grottoes, it's the very first step to characterize different sandstones. On this basis, this study aims to: (1) comprehensively analyze the petrophysical and mechanical properties of sandstones from representative Chinese grottoes; (2) find the key control influencing mechanical performance of the grotto sandstones; and (3) establish relationships between quantitative petrophysical properties and mechanical parameters.

Methods

Sampling and sample preparation

This study investigated four representative Chinese grotto sandstones (Table 1), selected for their historical significance and regional diversity. From each site, at least 20 samples were randomly collected, with their bedding plane orientations documented. Three sandstones (YG, LS, TLS) occur in thick layers of few meters, while DZ sandstone forms centimeter- to millimeter-scale thin layers.

All samples were precision-cut into standardized cylinder samples (Ø50 mm × 50 mm height) with end-faces parallel to bedding planes. Through ultrasonic P-wave velocity screening, we identified seven consistent specimens of each type of sandstones for detailed analysis. The specimens were assigned as follows: three of them were tested for the density, porosity, ultrasonic P-wave velocity, surface hardness, and uniaxial compressive strength (UCS); three of them were tested for capillarity water absorption; and one of them was for salt crystallization resistance test.

The Yungang Grottoes were carved 16 km west of Datong City in Shanxi Province starting 453 A.D. (Northern Wei Dynasty). Jurassic Yungang Formation, the strata where the grottoes were carved, is mainly comprises of medium- to coarse-grained quartz sandstone interlayered with mudstone and sandy mudstone²⁴. The Tianlongshan Grottoes are located in the Tianlong Mountain, approximately 36 km southwest of Taiyuan City in Shanxi Province. Tianlongshan Grottoes were first built during the Eastern Wei Dynasty (534–550 A.D.) and continued to be excavated and improved by the Northern Qi, Sui, Tang, and Ming dynasties over the next 500 years. The caves are situated at an altitude of around 1500 m and are composed of quartzose sandstone from Permian Tianlongsi Formation. Leshan Giant Buddha, the largest sitting statue of Maitreya Buddha in the world (71 m high), carved on the western cliff of Lingyun Mountain in Leshan City,

Sichuan Province during Tang Dynasty (618–907 A.D.). The outcrop of strata in this region is the lower part of the Upper Cretaceous Jiaguan Formation dominated by medium- to fine-grained red sandstone²⁵. The formation is mainly composed of red sandstone and mudstone intercalated layers. The Dazu Rock Carvings are located in Dazu District of Chongqing City. There are five major sites of rock carvings scattered in this area. The carvings are featured with harmonious coexistence of different religions (Buddhism, Confucianism and Taoism). Famous for The Niche of Sakymuni Entering Nirvana, Baoding Mountain is one of the most outstanding among the five sites. Hence, the sample in this study was extracted from Upper Jurassic Penglaizhen Formation of Baoding Mountain. The formation is mainly composed of medium- to fine-grained feldspar quartz sandstone and some mudstone intercalation with horizontal bedding and parallel bedding structure²⁶ (Fig. 1).

Petrographic and chemical analysis

Standard thin sections as well as casting thin sections with blue-dyed resins were prepared for each sandstone. Thin sections were prepared from adjacent portions of the same specimens used for mechanical testing, ensuring petrographic-mechanical data correspondence. Leica DM2700P polarized optical microscope was used to obtain petrographic indices characterizing composition and texture of samples. The composition of sandstones, including mineralogy and proportion of framework grains and cement, proportion of matrix and void, were measured according to the point-count method²⁷.

The packing density, contact type, and contact nature were determined for the four sandstones by counting along traverses in thin sections²⁸. Packing density quantifying the compactness of grains within the sandstones were calculated according to Kahn²⁹. The contact type and contact nature developed by Taylor³⁰, were counted to characterize how closely the grains are spatially arranged. Contact types include tangential contacts, long contacts, concavo-convex contacts and sutured contacts. Contact nature includes grain-to-grain contacts (G-G), grain-to-cement contacts (G-C), grain-to-matrix contacts (G-M) and grain-to-void contacts (G-V). Multiple indices were developed based on contacts of grains in sandstones, some most used are listed in Table 2.

Scanning electron microscopy (SEM) was done on the four raw sandstones with Regulus 8230 scanning electron microscope. This investigation focused on the presence of clay minerals in the binding cement of the sandstones. Energy dispersive X-ray (EDX) analyses were also employed to characterize the specific kinds of the observed clay minerals.

For further mineralogical characterization, sample preparation and X-Ray diffraction (XRD) test was conducted according to USGS laboratory manual³¹ and Chinese industry standard SY/T 5163-2018³². A Rigaku Ultima IV X-ray diffractometer with Cu K α radiation was used to qualitatively determine both the whole rock powder and clay minerals of the samples. The voltage and the current of the X-ray tube were 40 kV and 40 mA respectively. The profiles of the whole rock powder samples were recorded in the angular range of 5–70° with a step size of 0.02°, while the profiles of the clay minerals were recorded in the range of 2.5–30° with a step size of 0.02°.

The major and trace elements was recognized using the HORIBA's Ultima Expert Inductively Coupled Plasma Optical Emission Spectrometer (ICP-OES) according to Chinese national standard GB/T 14506.31-2019³³.

Table 1 | List of the four studied sandstones.

Sample	Abbreviation	Location	Era	Formation
Yungang sandstone	YG	Shanxi	Jurassic	Yungang Formation
Tianlongshan sandstone	TLS	Shanxi	Permian	Tianlongsi Formation
Leshan sandstone	LS	Sichuan	Cretaceous	Jiaguan Formation
Dazu sandstone	DZ	Chongqing	Jurassic	Suining Formation

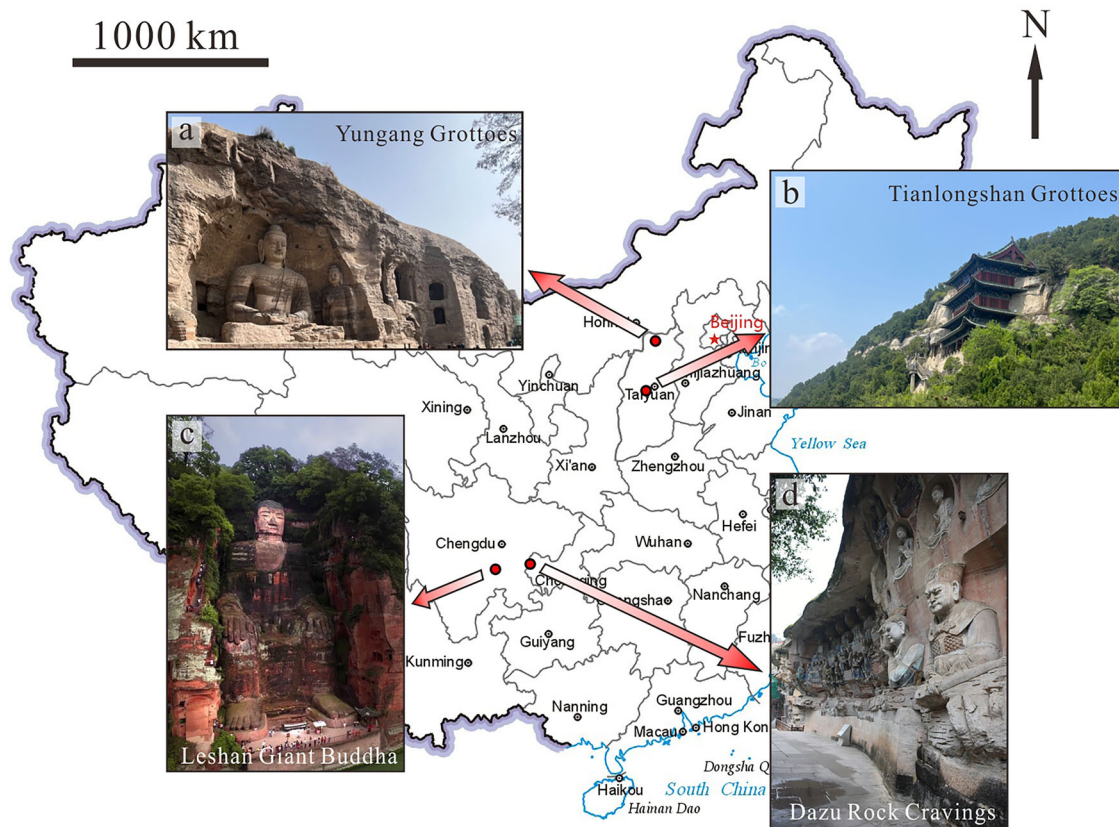


Fig. 1 | Locations of the four sandstone heritage sites in this study. a Yungang Grottoes, **b** Tianlongshan Grottoes, **c** Leshan Giant Buddha, and **d** Dazu Rock Carvings.

Table 2 | Summary of indices for grain contact (After Shakoor and Bonelli²⁰).

Indices	Description
GVCM	The average number of grain-to-grain contacts plus the average number of grain-to-cement contacts were divided by the average number of grain-to-void plus the average number grain-to-matrix contacts.
STPT	The average number of sutured contacts were divided by the average number of point contacts.
GV	The average number of cement-to-grain contacts were divided by the average number of void-to-grain contacts.
CCDC	The average number of sutured contacts plus the average number of concave-convex contacts were divided by the average number of point contacts plus the average number of straight contacts.
SOWC	The average number of sutured contacts plus grain-to-cement contacts were divided by the sum number of tangential contacts, long contacts, grain-to-void contacts, and grain-to-matrix contacts.

Physical properties analysis

To characterize pore size distribution on samples, mercury intrusion porosimetry (MIP) was conducted with Micromeritics AutoPore V 9620 mercury injection instrument on small fragments of about 1 g, according to Chinese national standard “The rock capillary pressure measurement (GB/T 29171-2023)³⁴”. Mercury acts as a non-wetting liquid and intrudes progressively smaller pores with increasing pressure. Pressure differences can be converted to pore throat diameters using the Washburn equation. The surface tension of mercury is 0.48 N/m, and the contact angle between mercury and the pore surface were set for 140°.

Capillary water absorption was measured on three individual cylindrical samples for each sandstone types using static capillarity procedure³⁵ by adding water manually to keep the water surface 2 mm above the sample bottom. The sandstone samples were oriented such that water migration proceeded perpendicular to bedding planes. The weights were measured every 5 min in the first hour, every 15 min in the second hour and the third hour, and every hour from the fourth hour onward. The results were expressed in terms of the capillary coefficient (EN 1925: 99³⁶).

The coefficients of thermal expansion (CTE) were measured by NETZSCH TMA 402 with one rectangular prism sample of dimension of 5 mm × 5 mm × 25 mm for each type of sandstones. The heating process starts at 25 °C and then continuously increase up to 1000 °C within 150 min. The strain variations during the process were recorded as dL/L₀.

Other physical properties were calculated according to correlative standards. Three samples were tested for determination of density and porosity. In detail, the real density is referred to the volume of the specimen with no voids and determined through the pycnometer method, while the apparent density is measured considering the presence of pores. Open porosity and total porosity were also tested and calculated afterwards according to ASTM C97/C97M³⁷.

Mechanical properties analysis

For the uniaxial compressive strength (UCS) tests, three standard cylindrical specimens of 50 mm in diameter and 50 mm in length with co-planar end-faces were used according to ASTM C170/C170M³⁸. The samples were dried in oven for over 24 h at 105 °C before testing. The compressive load was applied by a servo-hydraulic testing machine with a very stiff testing frame

Table 3 | Mineralogical composition of sandstones by XRD.

	YG	TLS	LS	DZ
Quartz	29.2	75.9	42.0	32.4
K-feldspar	9.9	0.0	9.5	7.9
Albite	0.0	20.2	22.5	38.0
Pyrite	0.0	0.1	0.0	0.0
Ankerite	0.0	0.0	0.0	0.0
Dolomite	0.0	0.0	0.0	0.0
Calcite	6.2	0.0	18.5	14.3
Hemite	0.3	0.0	0.8	0.4
Clays	54.5	3.8	6.8	7.0
I/S	2.5	62.0	—	—
Illite	8.4	19.2	42.7	23.0
Kaolinite	89.1	18.8	—	—
Chlorite	—	—	6.4	—
Smectite	—	—	50.9	—
C/S	—	—	—	77.0

I/S Illite-Smectite mixed-layer, C/S Chlorite-Smectite mixed-layer.

(3000 kN/mm) and the load ranges up to 300 kN. The load was applied to the end-faces of the specimen with a strain rate of 10^{-5} s⁻¹ until failure. The uniaxial compressive strength was determined from the maximum load.

Ultrasonic P-wave velocity and surface hardness were measured on the same dried cylindrical samples before UCS tests. Propagation times of ultrasonic pulses (piezoceramic transducers, resonant frequency 54 kHz) were measured in direction vertical to end-faces of the samples using the pulse transmission technique according to ASTM D2845-05³⁹. Surface hardness tests utilized the Equotip Piccolo 2 portable testing device, which works with the rebound method, which indirectly measures the loss of energy of an impact body. A total of 15 individual measurements were done for each sample and the mean value was calculated as Ulusay et al.⁴⁰ recommended.

To evaluate salt crystallization resistance, one cylindrical sample (5 cm diameter, 5 cm tall) for each type of sandstones were exposed to a solution of sodium sulfate decahydrate (mass fraction of 14%). The cycling was stopped at 30 cycles or when the samples disintegrated or fragmented into pieces each weighing <75% of the pre-test mass after final drying (EN 12370: 2020⁴¹).

Results

Petrographic and chemical properties

A summary of the minerals and their ratios to characterize the lithology and sandstone composition are presented in Table 3. A comparison of thin section, XRD, and ICP-OES data show reasonably close matches between the profiles of SiO₂ and quartz, Na₂O and plagioclase, K₂O and K-feldspar, and CaO and Calcite, etc., providing further evidence for these as probable element-mineral affinities.

Yungang sandstone (YG) is featured with poor sorting and abundant kaolinite composition. Petrographic analysis shows that the Yungang sandstone is massive, medium to coarse grained litho-feldspatho-quartzose sandstone with an average composition of Q₅₀F₃₀L₂₀. Most grains are subangular and the sizes are mostly 0.2–1.8 mm. Many feldspars were metamorphosized (Fig. 2a, b). The lithic fragments are mostly quartzite and chert; slate compositions can also be identified in particular thin sections. A considerable amount of heavy minerals such as garnet, magnetite, etc. has also been identified. The interstitial material is dominated with significant amount of kaolinite (Fig. 2c).

Tianlongshan sandstone (TLS) is massive, well-sorted, gray-greenish feldspatho-quartzose sandstone with grain sizes range within 0.2–1.0 mm. The grains are mainly terrigenous, and the interstitial content is about 10%.

Most of the grains are, circular to subcircular, and a small amount is sub-angular, with a particle size of 0.2–0.5 mm. The composition of the grains is quartz (75–80%), feldspar (10–15%), rock fragment (ca. 10%), with a trace amount of muscovite. The feldspar is dominate with albite (ca. 20%), whereas K-feldspar (5%) are mostly replaced by clay minerals (Fig. 2d, e; Fig. 3). Some grains are partly covered by hematite coatings or a mixture of ferric cement (iron oxides or iron hydroxide) and clay minerals (probably smectite, illite, or I/S mix layer; Fig. 2f).

Leshan red sandstone (LS) is massive, fine-grained, moderately sorted, and light reddish to pink colored feldspatho-quartzose sandstone. The grain sizes ranging from 0.05 to 0.25 mm. Mineralogically, quartz (50%) and feldspar (45%) comprise of the major framework (Fig. 3), while minor muscovite occurs unevenly distributed as singular flakes (about 5%). The grains generally show a shape ranging from rounded to subangular, except for few well-preserved euhedral crystals (Fig. 2g, h). Elongated quartz or feldspar does not show any orientation, which suggests poor compaction. The interstitial materials are mainly calcite, clay minerals (Fig. 2i), and hematite.

Laminated structure caused by goethite and different grain size is observable in Dazu sandstone (DZ). Grains are well-sorted very fine sand and coarse silt, with the particle size of mostly 0.1–0.3 mm (concentrated in 0.1–0.2 mm). Grains are mainly crystal, and the content of interstitial material is about 10%. Most of the grains show sub-angular to sub-circular in shape, a small amount is circular (Fig. 2j, k). The grains comprise of quartz (65–75%), feldspar (20–30%), and a small amount of muscovite (about 5%). The interstitial material is mainly calcite and clay minerals (mainly fibrous illite or interstratified illite-chlorite) (Fig. 2l, 4), also a small amount of goethite.

The petrographic indices included tangential contact, long contact, concavo-convex contact, sutured contact, G-G contact, G-C contact, G-M contact, G-V contact, GVCM, STPT, CV, CCDC, SOWC, and packing density (Pd) (Table 2). The calculations of the parameters were listed in Table 4.

Major elements can be reliable indicators of the provenance of sediments, therefore profound distinguish features for sandstones. Apart from singular elements, multiple indices have been developed to estimate the weathering levels based on ratios of unstable and relatively stable element oxides, for instance, chemical index of alteration⁴² and chemical index of weathering⁴³. The chemical characteristics of the sandstones were listed in Table 5. YG is signature with low SiO₂/Al₂O₃ and high Na₂O/K₂O ratios that indicate graywacke compositions⁴⁴. The high Al₂O₃ percentage is the proof of the abundant content of kaolinite and the high K₂O/Na₂O ratio is corresponded with K-feldspar dominant over plagioclase. Relative low mica contents and rare heavy minerals comprising a resistant suite. TLS is characterized by high SiO₂ (88.26 wt.%), low Al₂O₃ (6.80 wt.%), and corresponded high quartz content (ca. 76%). The feldspar is dominate with albite (ca. 20%), whereas K-feldspar are mostly replaced by clay minerals. LS and DZ have similar major elements composition, which are characterized by a slightly lower SiO₂ (73.37 wt.% and 75.13 wt.%), high CaO (7.21 wt.% and 8.26 wt.%).

Physical and mechanical properties

According to the combined observations of thin section and SEM, the pore types of the sandstones can be sorted into five types: intergranular pores, intragranular pores, dissolution pores (intergranular and intragranular), micropores closely related to clay aggregates, and microfractures (Fig. 5). Residual primary intergranular pores which were developed at early stage of diagenesis between mineral grains, are mainly affected by compaction, cementation and tectonic extrusion. The long axis of this kind of pores with straight pore edge and clear boundary ranges from 20 to 100 μ m, even several hundred microns, and the minor axis ranges between 10 and 50 μ m.

Pores in YG sandstone are intragranular pores, dissolved pores, micropores of clay minerals, and microfractures (Fig. 5a). In TLS sandstone, the pores are mostly intergranular pores, intragranular pores, dissolved pores, and micropores of clay minerals (Fig. 5b–e). Whereas in LS and DZ

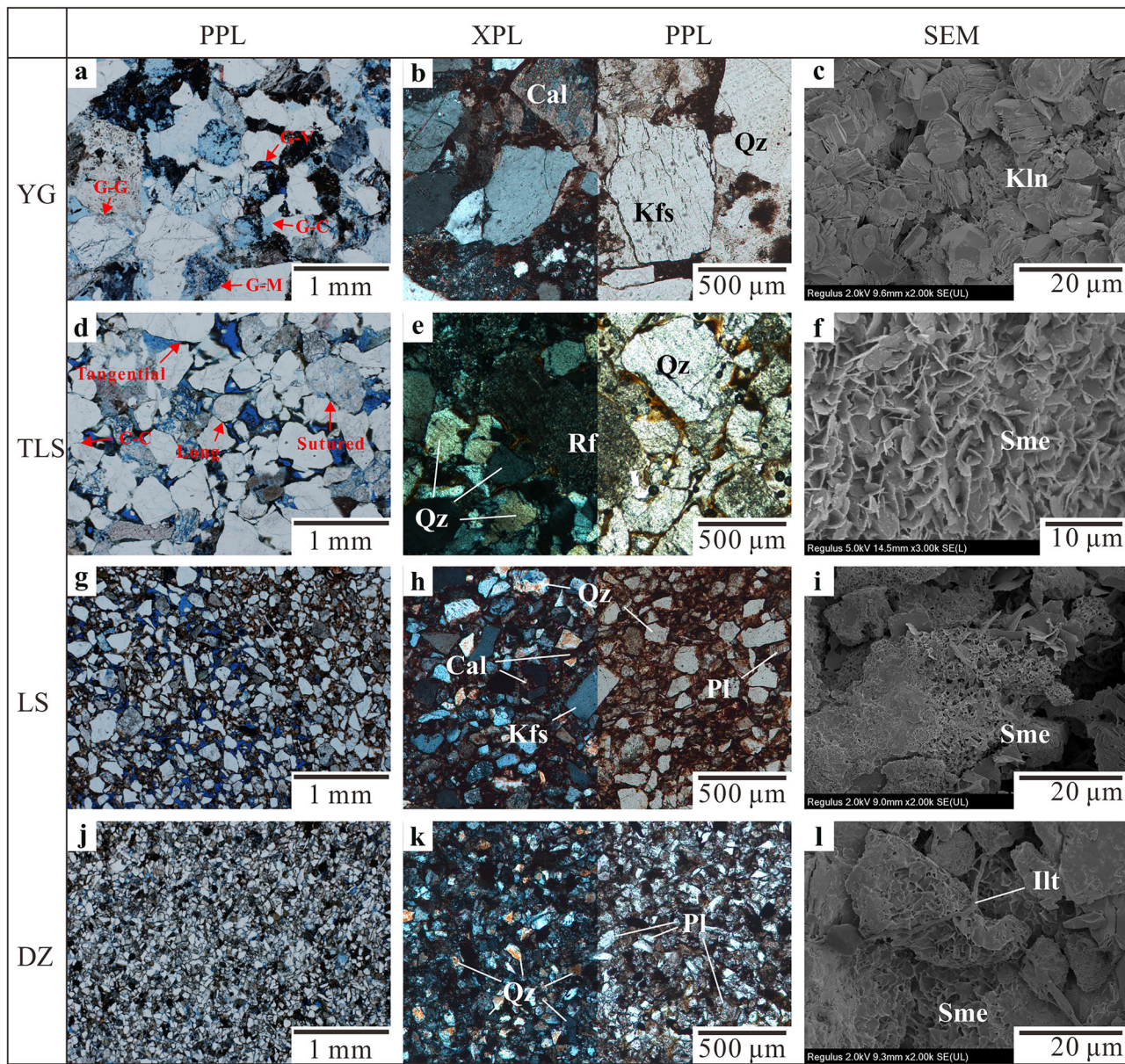


Fig. 2 | Micrographs of thin sections and secondary electron images of the sandstones. a, d, g, j Micrographs of cast thin sections under plane polarized light. b, e, h, k Micrographs of standard thin sections under both cross polarized light and plane polarized light. c, f, i, l Secondary electron images. PPL = plane polarized light; XPL = cross polarized light. The abbreviations were adapted after Whitney and

Evans⁵⁴ (Qz = Quartz; Kfs = K-feldspar; Pl = Plagioclase; Cal = Calcite; Rf = Rock fragment; Kln = Kaolinite; Sme = Smectite; Ilt = Illite). Contact nature was shown on micrographs of cast thin sections of YG sandstone (a); contact types, including tangential contact, long contact, concavo-convex (C-C), and sutured contact, were shown on casting section photo of TLS sandstone (d).

sandstone, the pores are mostly intergranular pores and micropores closely related to clay aggregates. The physical properties measured in this study are given in Table 6. The total porosity of sandstones measured range from 8 to 12%. The Green sandstone from Tianlongshan Grotto (TLS) is the one with the highest porosity (12.10%) while Yungang sandstone (YG) is the one with lowest porosity (7.90%). The porosities of Leshan sandstone (LS, 11.59%) and Dazu sandstone (DZ, 11.17%) are comparable. DZ is with a unimodal distribution, YG has an unequal unimodal pores size distribution, whereas TLS and LS are with multimodal distribution.

The large portion of macro pores (diameter >0.1 mm) in Leshan sandstone might be the main reason of the high porosity tested. Ondrášík and Kopecký proposed that pores in stones could be divided into nanopores (diameter <0.05 μm), micropores (0.05 μm $<$ diameter <100 μm) and macropores (100 μm $<$ diameter <1000 μm)⁴⁵. Log differential intrusion volumes of mercury against pore size diameters of four sandstone samples

are plotted in Fig. 6. It can be observed that there is one peak for Yungang and Dazu sandstones, two peaks for Leshan sandstone, and Tianlongshan sandstone shows approximate three peak points.

Capillarity water absorption tests were carried out over a long period (over 60 h). At saturation the YG absorbs 4502 g/m² of water, the TLS 5680 g/m², the LS 5842 g/m² and DZ more than 4894 g/m². The water absorption coefficients of the four sandstones are therefore calculated to be 1.11 kg/m²/h^{0.5} for YG, 1.44 kg/m²/h^{0.5} for TLS, 1.81 kg/m²/h^{0.5} for LS, and 0.80 kg/m²/h^{0.5} for DZ (Fig. 7).

The thermal expansions of the four sandstones show considerable differences. Based on thermal expansion characteristics, the four sandstones can be classified into two groups, YG and TLS, DZ and LS. The thermal expansion coefficient-temperature curve is similar before 700 °C, gradually increasing linearly from 0 to 0.00003 within the 25–500°C range. All sandstones show similar thermal expansion at 60 °C with approximately

Fig. 3 | Whole rock XRD patterns of four sandstones.

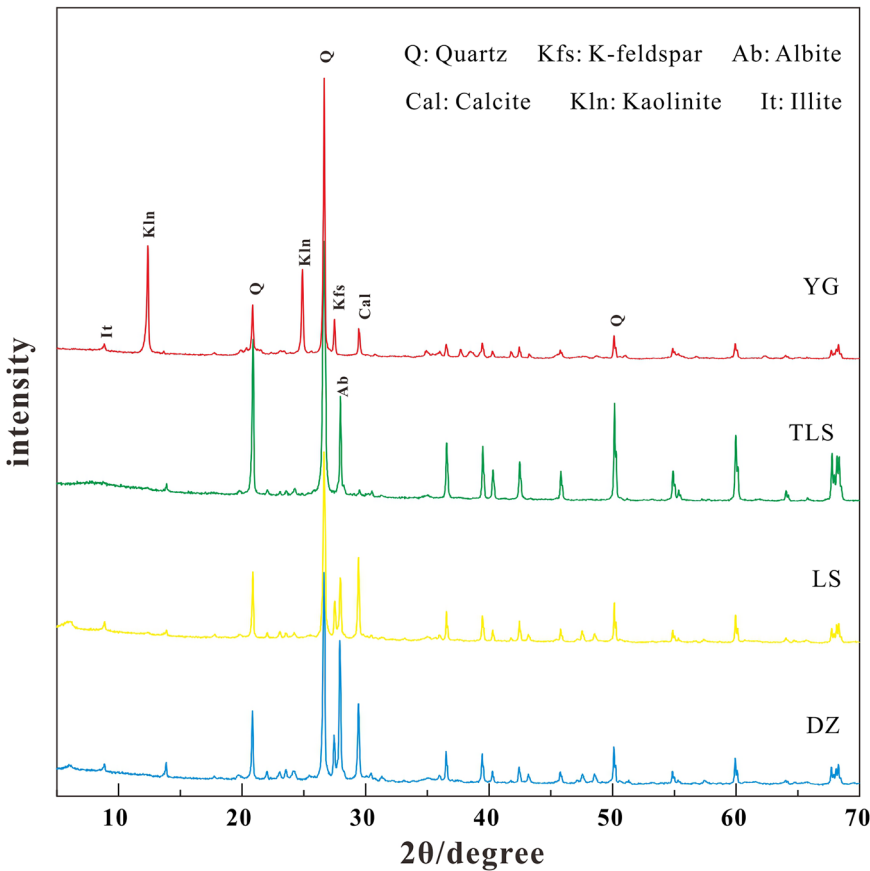
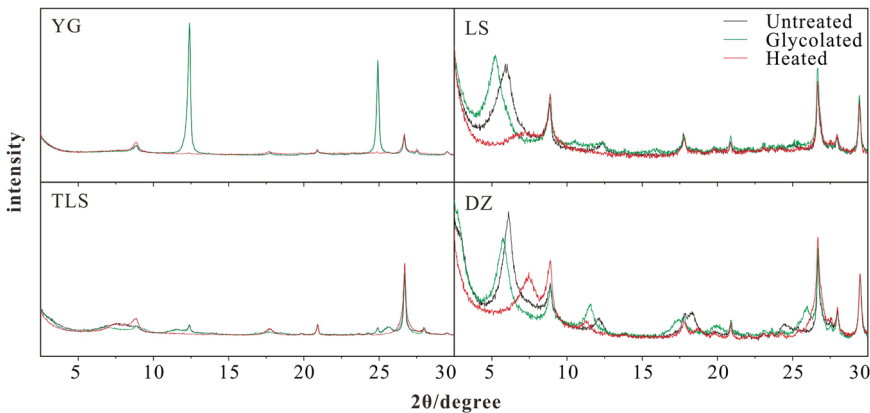


Fig. 4 | XRD patterns of clay minerals of four sandstones under untreated (natural oriented), glycolated, and heated ($550\text{ }^{\circ}\text{C}$) conditions.



0.30 mm/m. The dilation rapidly rises to around 0.00010 between 500 and $565\text{ }^{\circ}\text{C}$, and then decreases linearly. The expansion almost stops at around $600\text{ }^{\circ}\text{C}$. Subsequently, YG and TLS maintain a constant coefficient of thermal expansion (CTE), while DZ and LS continue to slowly expand after $750\text{ }^{\circ}\text{C}$, with fluctuations in the thermal expansion coefficient.

The apparent density of the four samples ranges between 2.32 and 2.42 g/cm^3 (Table 6). The Yungang sandstone attains the highest value with 2.42 g/cm^3 . The lowest value is shown by the red sandstone of Leshan, having a value of 2.32 g/cm^3 . Porosity of the samples varies from 7.90 to 12.10%. The one with the lowest porosity is YG (Table 6). Uniaxial compressive strength (UCS) of the sandstones ranges from 26 to 65 MPa. YG sandstone and DZ sandstone are strong (approximately 60 MPa), while TLS sandstone and LS sandstone are weak to moderately strong (33–43 MPa). For the four samples, the ultrasonic P-wave velocity ranges between 1714

and 2726 m/s under dry conditions (Table 6). Surface hardness of all samples ranges from 449 to 615 HLD (Table 6).

Salt resistance testing revealed distinct weathering behaviors among the four sandstones (Fig. 8). Initially, all samples showed minimal weight variation before experiencing dramatic changes. The number of cycles required to reach 25% weight loss ranged from 7 to 22. YG sandstone exhibited gradual edge deterioration beginning at the 10th cycle, with grain-by-grain loss culminating in 25% material loss by the 22nd cycle. In stark contrast, TLS sandstone demonstrated extreme vulnerability, with material loss initiating at the 6th cycle and reaching approximately 80% weight loss by the 7th cycle. LS sandstone maintained stability for the first 8 cycles before developing visible cracks and discoloration that progressed to severe weight loss. DZ sandstone displayed color changes (grayish to brownish) and developed surface-parallel cracks at the 12th

Table 4 | Sandstone indices related to textures of the samples.

		YG	TLS	LS	DZ
Contact Type	Tangential	4.5	30.3	45.5	8.3
	Long	53.6	35.9	35.9	67.3
	Concavo-convex	27.7	26.1	18.6	21.5
	Sutured	14.3	7.7	0.0	2.9
Contact Nature	G-G	28.0	35.5	18.1	60.4
	G-C	63.5	8.0	33.4	15.0
	G-M	5.3	4.3	16.0	13.0
	G-V	3.3	52.3	32.5	11.6
Petrographic Index	GVCM	10.8	0.8	1.1	3.1
	STPT	3.2	0.3	0.0	0.4
	CV	19.5	0.2	1.0	1.3
	CCDC	0.7	0.5	0.2	0.3
	SOWC	3.0	0.3	0.6	0.4
	Packing density	62.4	78.4	69.7	85.3

G-G grain-to-grain contact, G-C grain-to-cement contact, G-M grain-to-matrix contact, G-V grain-to-void contact.

Table 5 | Geochemical (ICP-OES) composition of the sandstones.

	Yungang sandstone	Tianlongshan sandstone	Leshan sandstone	Dazu sandstone
SiO ₂	79.98	88.26	73.37	75.13
Al ₂ O ₃	12.15	6.80	10.47	8.92
Fe ₂ O ₃	2.19	2.07	2.76	2.65
TiO ₂	0.28	0.16	0.52	0.47
MnO	0.22	0.28	1.24	1.22
MgO	0.07	0.05	0.08	0.05
CaO	3.01	0.37	7.21	8.26
Na ₂ O	0.22	1.15	2.56	1.58
K ₂ O	1.82	0.83	1.68	1.63
P ₂ O ₅	0.07	0.03	0.11	0.09
K ₂ O/Na ₂ O	8.32	0.72	0.66	1.04
SiO ₂ /Al ₂ O ₃	6.58	12.98	7.01	8.42
CIA	56.92	62.36	33.87	30.17
CIW	67.59	72.51	37.66	33.60

cycle, reached 25% weight loss at 16th cycle, ultimately forming contour scaling (Fig. 8).

Discussion

The porosity and pore structure have direct effect on most of the physical and mechanical properties of sandstones, with higher porosity typically resulting in weaker mechanical strength. Numerous researches, including data provided in this study, proved that the UCS of rock is controlled by porosity and density^{19,20,46–48} (Fig. 9). In the studied sandstones, porosity shows a clear inverse correlation with density due to their composition of light minerals with similar real densities (Table 6). These pore characteristics also govern salt crystallization resistance (SCR) by controlling salt transport and distribution²². For the four sandstones in this study, the salt crystallization resistance (SCR) has a liner negative correlation with the open porosity and

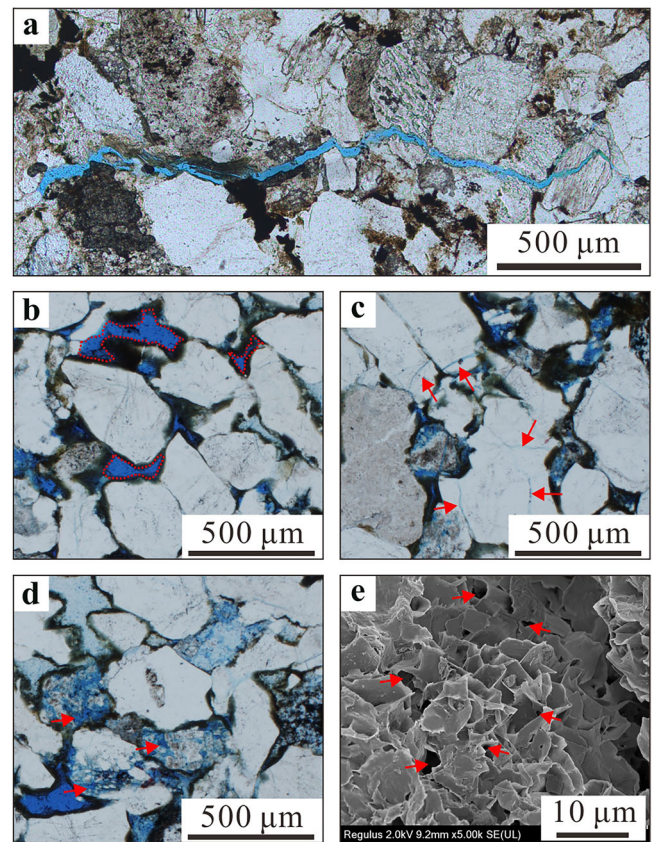


Fig. 5 | Pore types of the sandstones. **a** Microfractures in Yungang sandstone, **b** intergranular pores in Tianlongshan sandstone, **c** intragranular pores in Tianlongshan sandstone, **d** dissolution pores in Tianlongshan sandstone, and **e** micropores closely related to clay aggregates in Tianlongshan sandstone.

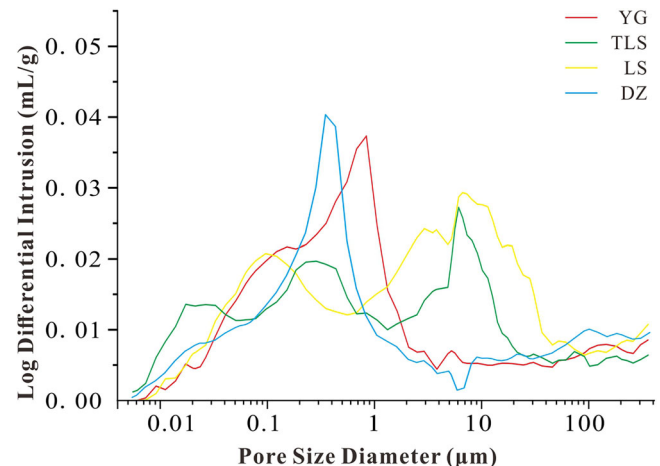


Fig. 6 | Pore size diameter measured by MIP.

sandstones with unimodal distribution (YG and DZ) have better performance than sandstones with multimodal distribution (TLS and LS).

It has been concluded that in sandstones, ultrasonic P-wave velocity and UCS exhibit a linearly positive correlation⁴⁹. In this study, the ultrasonic P-wave velocity and UCS also exhibit a positive correlation (Fig. 10a). Wedekind et al. gave a correlation of surface hardness (HLD) and compressive strength for chalkstone and tuff⁵⁰. But in sandstones studied in this paper, the texture results in the unclear correlation between them (Fig. 10b).

The relationship between composition characteristics and mechanical parameters in sandstones have been studied and discussed over decades. However, the studies on different cases lead to contradictory conclusions. For instance, Zorlu et al.^{15,23} found that quartz content and UCS have a positive correlation, whereas Shakoor and Bonelli²⁰ acquired a negative correlation. This infers that there is not always a definitive relationship between various mechanical properties and grain composition, particularly when the sandstones of different regions are concerned, as they have experienced different diagenesis and weathering processes. In this study, a

negative correlation was found between quartz weight percentage and uniaxial compression strength concerning four investigated sandstones. However, if it is the ratio of quartz and total grains that we concerned, the correlation cannot be obtained. Tianlongshan sandstone has the highest quartz content, but ends up with the poorest mechanical performance, which suggests the dominance of cementation and grain contact over grain composition. The components of sandstones (both major elements and minerals) exhibit similarities, yet their quantities can vary significantly depending on the origin and diagenesis. Geochemical and mineralogical data from sandstones can be reliable indicators of the provenance of sediments and profound distinguishing features for sandstones, but not suitable properties to predict strength and durability.

The thermal expansion coefficient of a stone is closely related to mineralogy²⁸. As shown in Fig. 11, the thermal expansion coefficient peaks at 565°C probably for two reasons: (1) the crystallization of mineral components and the loss of structural water; and (2) the generation of macroscopic cracks inside the sample, i.e., the occurrence of thermal damage⁵¹. The difference between two groups might related to the variation of sizes and types of grains⁵². According to the thermal expansion properties of minerals, the larger proportion of feldspar contents in LS and DZ sandstones is the dominant factor leading to the continues expansion after the phase transition of quartz (Fig. 11). Thermal expansion is a commonly studied property in understanding stone durability, hence, it is a universal but important feature for characterizing different sandstones^{52,53}.

Cementation between the grains plays a crucial role in determining sandstone mechanical strength, where strong cements (e.g., siliceous and calcite) enhance compressive strength, while weak clay mineral cements reduce it². The major differences in the cementation of the four sandstones analyzed are linked to the quantity and composition of clay minerals (54.5% for YG, 3.8% for TLS, 6.8% for LS, and 7.0% for DZ) and to the amount of calcite (6.2% for YG, 18.5% for LS, 14.3% for DZ, and none was detected for

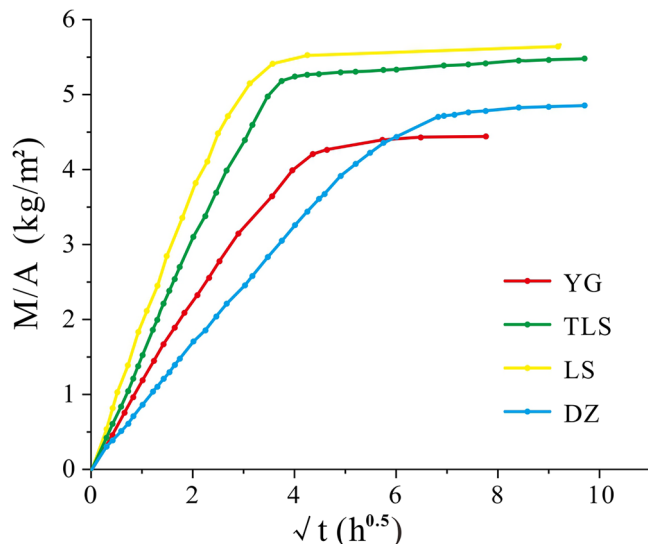


Fig. 7 | Capillary water absorption curves for the four sandstones.

Table 6 | Basic physical and mechanical characteristics of the four sandstones.

Sandstones	YG	TLS	LS	DZ	
Apparent density (g/cm ³)	Mean ± SD	2.42 ± 0.01	2.32 ± 0.00	2.34 ± 0.01	2.40 ± 0.00
Real density (g/cm ³)	Mean ± SD	2.64 ± 0.01	2.65 ± 0.00	2.64 ± 0.01	2.69 ± 0.00
Open porosity (%)	Mean ± SD	7.62 ± 0.15	10.81 ± 0.19	10.24 ± 0.15	8.43 ± 0.24
Total porosity (%)	Mean ± SD	7.90 ± 0.26	12.10 ± 0.11	11.59 ± 0.45	11.17 ± 0.49
UCS (MPa)	Mean ± SD	58.7 ± 5.2	33.2 ± 6.0	43.5 ± 3.6	62.2 ± 1.1
Vp (m/s)	Mean ± SD	2633 ± 67	1741 ± 24	1967 ± 28	2651 ± 11
Surface Hardness (HLD)	Mean ± SD	518 ± 59	576 ± 22	569 ± 7	603 ± 8

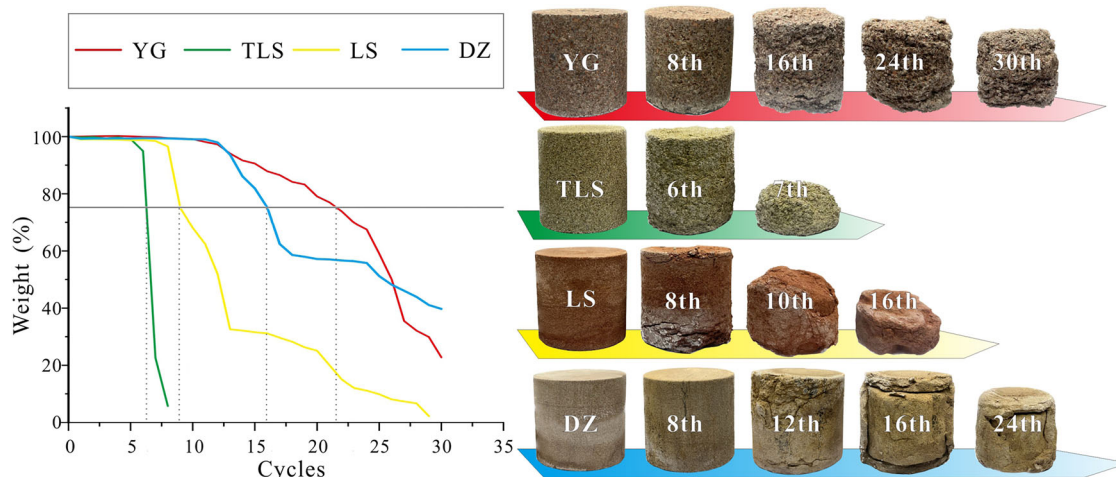


Fig. 8 | Salt crystallization resistance test performed on the four sandstones.

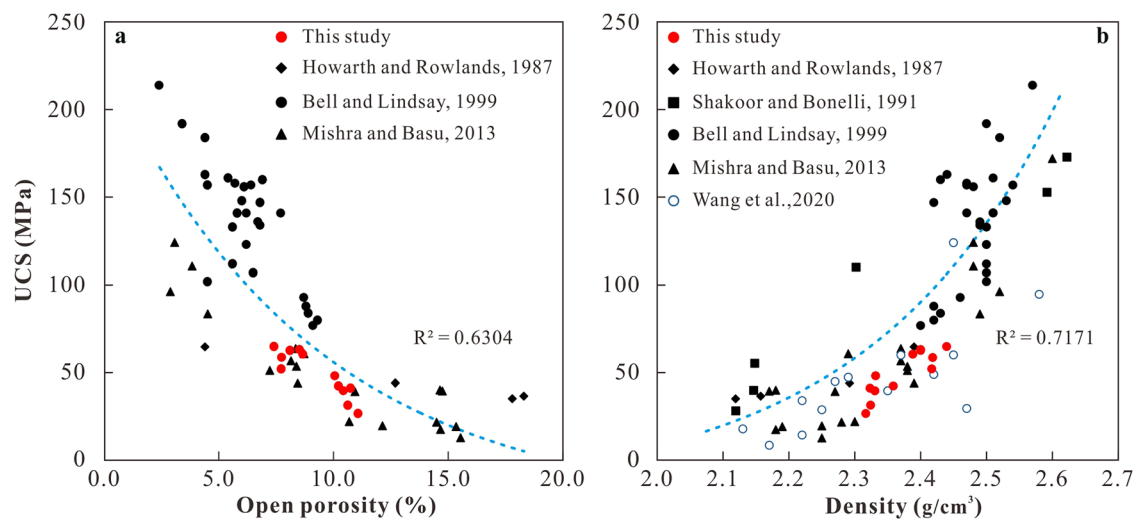


Fig. 9 | Correlation of physical parameters to uniaxial compressive strength (UCS) of sandstones. **a** Open porosity to UCS and **b** density to UCS.

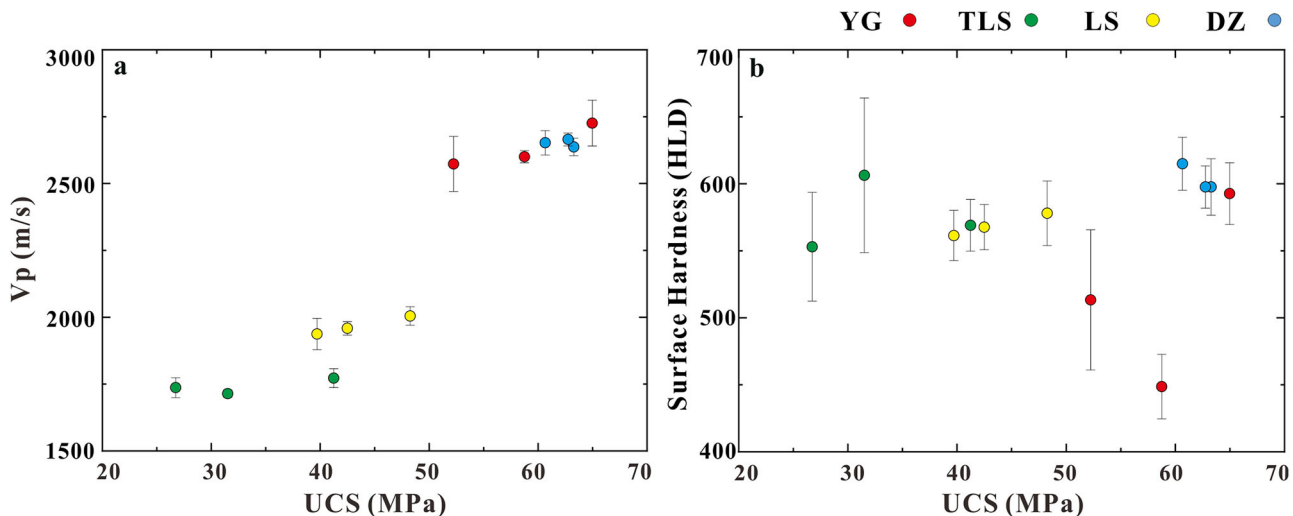


Fig. 10 | Correlation of ultrasonic P-wave velocity to uniaxial compressive strength (UCS) of the four sandstones. **a** Correlation of ultrasonic P-wave velocity to UCS and **b** Surface hardness to UCS.

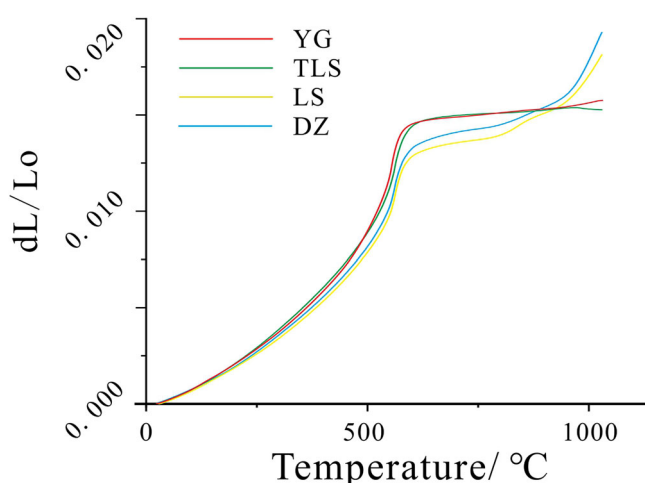


Fig. 11 | Thermal expansion properties of sandstone samples during heating process.

YG sandstone exhibits exceptional kaolinite content (48%) predominantly filling intergranular pores (Fig. 2a). The high kaolinite content and well compaction led to the relatively low porosity and good mechanical performance of YG sandstone. In contrast, TLS, LS and DZ sandstones contain smectite, illite, and chlorite that promote hydric expansion, reducing weathering durability and salt crystallization resistance.

Sandstone texture, defined by the arrangement of grains and cement, significantly influences mechanical behavior. Three key textural parameters were quantitatively characterized: contact types, contact nature, and petrographic indices. While three contact ratios (grain-grain, grain-cement, and grain-matrix) showed no correlation with strength (Fig. 12a–c), grain-void contact demonstrated a negative correlation (Fig. 12d), as it directly reflects visible pore space in thin sections. Among various petrographic indices, the GVCM index—incorporating all four contact types (G-G, G-C, G-V, G-M) (Table 2)—showed the strongest correlations: $R^2 = 0.7426$ with strength and $R^2 = 0.8318$ with P-wave velocity (Fig. 12e, f).

In summary, the four studied sandstones can be classified into two distinct groups based on their petrophysical and mechanical characteristics: (1) high-performance sandstones (YG and DZ) featuring lower porosity (7.6–8.4%), unimodal pore-size distribution, superior cementation quality,

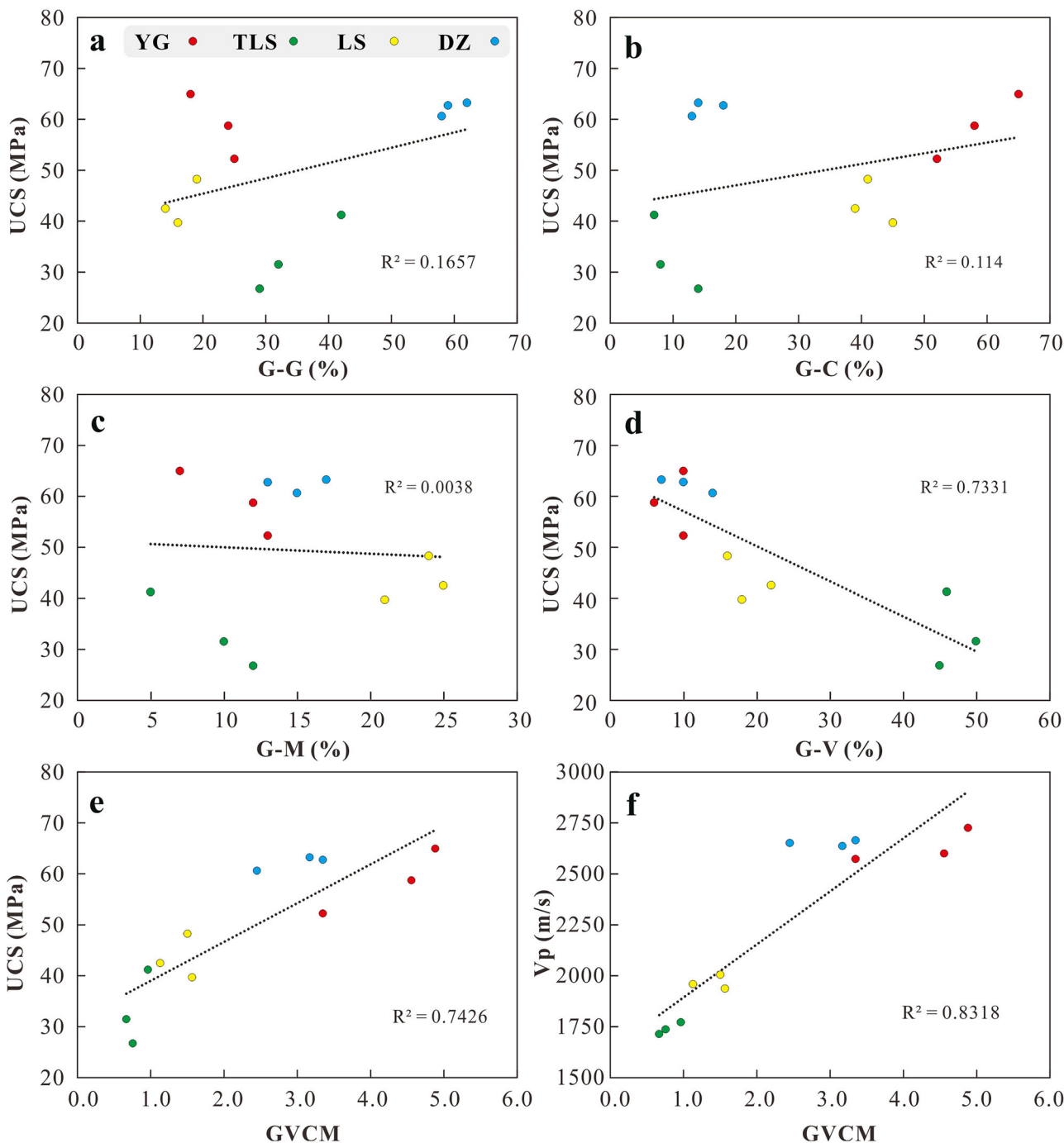


Fig. 12 | Correlations of mechanical properties to petrographic parameters. **a** UCS to grain-to-grain (G-G) contact ratio. **b** UCS to grain-to-cement (G-C) contact ratio. **c** UCS to grain-to-matrix (G-M) contact ratio. **d** UCS to grain-to-void (G-V) contact ratio. **e** UCS to GVCM index. **f** Ultrasonic P-wave velocity to GVCM index.

and consequently higher P-wave velocity (>2600 m/s), UCS (>58 MPa), and GVCM (generally over 3.0) values; and (2) low-performance sandstones (TLS and LS) showing higher porosity (10.4%–10.8%), multimodal pore-size distribution, weaker cementation, leading to reduced P-wave velocity (<2000 m/s), UCS (< 44 MPa), and GVCM (below 2.0) values, ultimately resulting in greater weathering susceptibility.

Yungang Grottoes and Tianlongshan Grottoes located in northern China, where the climate is relatively dry. The most common weathering form is near-surface weathering associated with intense day-night and seasonal temperature variations. (Fig. 13a, b). In southeastern China, the Leshan Giant Buddha and the Dazu Rock Carvings experience a subtropical climate with high temperature and precipitation, along with short sunshine

hours (Fig. 14), results in prolonged surface moisture retention on cultural heritage after rainfall events. Under these conditions, LS sandstone is highly susceptible to wet-dry cycling, where repeated absorption and evaporation of water accompanied with crystallization and dissolution of soluble salts accelerating surface weathering. Constant expansion and shrinkage contributed to severe sugaring or scaling in LS sandstones (Fig. 13c, d), regarding to considerable swellable clay minerals (smectite and illite). The divergence of regional climates significantly compounds the weathering conditions in grottoes with distinct lithologies. For future conservation work, it is also essential to develop compatible consolidation materials that are compatible to the physical and chemical properties of the sandstone. The formulations and dimensions of the material should be flexibly customized

Fig. 13 | Weathering forms of the four grottoes.
a Yungang Grottoes, **b** Tianlongshan Grottoes, **c** Leshan Giant Buddha, and **d** Dazu Rock Carvings.

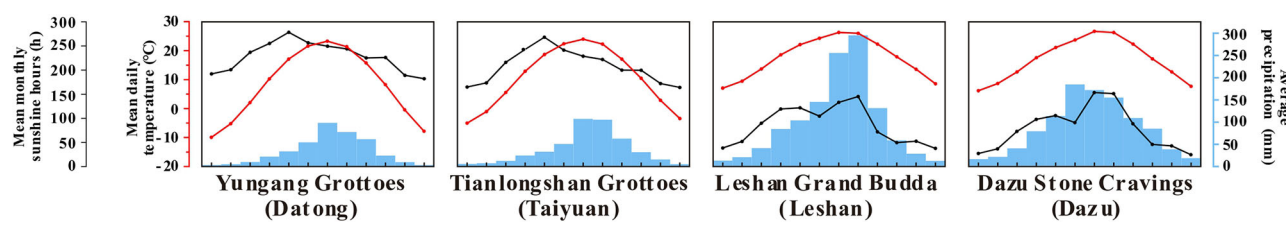
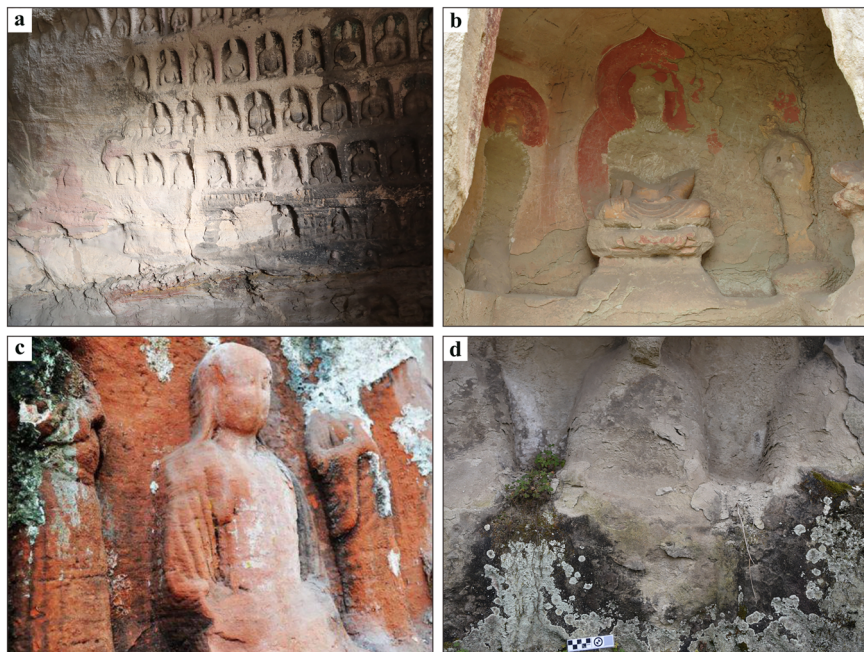


Fig. 14 | Mean temperatures, mean monthly sunshine hours, and average precipitation of the sandstone heritages.

to be compatible with the specific characteristics of each heritage sandstone, with material designs optimized based on porosity, cement types, thermal expansion, etc.

This study conducted comprehensive physical and petrographic characterization of four iconic sandstone grottoes in China, revealing key insights into their mechanical behavior.

- While grain types and geochemical compositions showed no direct correlation with mechanical properties—remaining stable markers of origin and diagenesis—porosity and density exhibited clear relationships with strength.
- Porosity is the key control of the sandstone strength. Sandstones with lower porosity and few pores of 1–100 µm (YG, DZ) demonstrated superior strength to those with higher porosity and massive pores of 1–100 µm (TLS, LS).
- Petrographic analysis further established that mechanical properties are governed by grain contact patterns and cementation types. Quantitative petrographic index like GVCM can be used when predicting sandstone strength.

Data availability

The datasets used and presented in this study are available from the corresponding author upon reasonable request.

Received: 28 April 2025; Accepted: 12 September 2025;

Published online: 30 September 2025

References

- Meybeck, M. Global chemical weathering of surficial rocks estimated from river dissolved loads. *Am. J. Sci.* **287**, 401–428 (1987).
- Stone in Architecture: Properties, Durability.* (Springer Berlin Heidelberg, Berlin, Heidelberg). <https://doi.org/10.1007/978-3-642-14475-2>. (2011).
- Huang, J.-Z. et al. Recent progresses in sandstone cave temples conservation: A case study of Yungang Grottoes. *Southeast Cult.* **261**, 15–19 (2018).
- Wang, J. & Huo, X. A discussion on the key scientific and technological issues in cave temples protection. *Southeast Cult.* **279**, 6–13 (2021).
- Lan, H. et al. Advances in degradation and instability mechanism of Grotto Temple Rock Mass. *Earth Sci.* **48**, 1603–1633 (2023).
- Hoffmann, A. Naturwerksteine Thailands: Lagerstättenerkundung und Bewertung. <https://doi.org/10.53846/goediss-2417> (2006).
- Stück, H., Koch, R. & Siegesmund, S. Petrographical and petrophysical properties of sandstones: statistical analysis as an approach to predict material behaviour and construction suitability. *Environ. Earth Sci.* **69**, 1299–1332 (2013).
- Wedekind, W., Gross, C. J., Hoffmann, A. & Siegesmund, S. Damage phenomenon and petrophysical properties of sandstones at the Phnom Bakheng Temple (Angkor, Cambodia): first investigations and possible conservation measures. *Environ. Earth Sci.* **77**, 735 (2018).
- Hoffmann, D., Niesel, K. & Plagge, R. Relationship between pore structure and other physico-technical characteristics of stone. in

Proceedings of the 8th International Congress on Deterioration and Conservation of Stone 461–172 (Berlin, Germany, 1996).

10. Wang, Y. et al. Quantitative evaluation of alteration and exfoliation in Jurassic sandstone, Chongqing Danzishi rock carvings, China. *Eng. Geol.* **292**, 106277 (2021).
11. Fang, Z. et al. Application of non-destructive test results to estimate rock mechanical characteristics—a case study. *Minerals* **13**, 472 (2023).
12. Katz, O., Reches, Z. & Roegiers, J.-C. Evaluation of mechanical rock properties using a Schmidt Hammer. *Int. J. Rock. Mech. Min. Sci.* **37**, 723–728 (2000).
13. Shalabi, F. I., Cording, E. J. & Al-Hattamleh, O. H. Estimation of rock engineering properties using hardness tests. *Eng. Geol.* **90**, 138–147 (2007).
14. Lin, S. et al. Cross-scale quantitative and qualitative study of Grotto sandstone under salt weathering. *Rock. Mech. Rock. Eng.* **57**, 10953–10971 (2024).
15. Zorlu, K., Ulusay, R., Ocakoglu, F., Gokceoglu, C. & Sonmez, H. Predicting intact rock properties of selected sandstones using petrographic thin-section data. *Int. J. Rock. Mech. Min. Sci.* **41**, 93–98 (2004).
16. Tandon, R. S. & Gupta, V. The control of mineral constituents and textural characteristics on the petrophysical & mechanical (PM) properties of different rocks of the Himalaya. *Eng. Geol.* **153**, 125–143 (2013).
17. Cantisani, E., Garzonio, C. A., Ricci, M. & Vettori, S. Relationships between the petrographical, physical and mechanical properties of some Italian sandstones. *Int. J. Rock. Mech. Min. Sci.* **60**, 321–332 (2013).
18. Ulusay, R., Türeli, K. & Ider, M. H. Prediction of engineering properties of a selected litharenite sandstone from its petrographic characteristics using correlation and multivariate statistical techniques. *Eng. Geol.* **38**, 135–157 (1994).
19. Wang, Z. et al. Relationship between petrographic parameters and physical-mechanical properties of weakly cemented sandstones. *QJEGH* **54**, qjegh2018-168 (2020).
20. Shakoor, A. & Bonelli, R. E. Relationship between petrographic characteristics, engineering index properties, and mechanical properties of selected sandstones. *Environ. Eng. Geosci.* **XXVIII**, 55–71 (1991).
21. Bjørlykke, K. Relationships between depositional environments, burial history and rock properties. Some principal aspects of diagenetic process in sedimentary basins. *Sediment. Geol.* **301**, 1–14 (2014).
22. Bourgès, A. Holistic correlation of physical and mechanical properties of selected natural stones for assessing durability and weathering in the natural environment. (Ludwigs-Maximilians-Universität München, 2006).
23. Zorlu, K., Gokceoglu, C., Ocakoglu, F., Nefeslioglu, H. A. & Acikalin, S. Prediction of uniaxial compressive strength of sandstones using petrography-based models. *Eng. Geol.* **96**, 141–158 (2008).
24. Guo, F. & Jiang, G. Investigation into rock moisture and salinity regimes: implications of sandstone weathering in Yungang Grottoes, China. *Carbonates Evaporites* **30**, 1–11 (2015).
25. Xie, L., Zhang, B. & Hu, Y. A novel method of preparing a standard weathered sandstone specimen: A case study of red sandstone from the Leshan Giant Buddha (Sichuan, China). *Int. J. Archit. Herit.* **17**, 538–552 (2021).
26. Zhang, J. et al. Surface weathering characteristics and degree of Niche of Sakyamuni Entering Nirvana at Dazu Rock Carvings, China. *Bull. Eng. Geol. Environ.* **78**, 3891–3899 (2019).
27. Hutchison, C. S. Laboratory handbook of petrographic techniques. *Mineral. Mag.* **40**, 111–112 (1975).
28. Ingersoll, R. V. et al. The effect of grain size on detrital modes: a test of the Gazzi-Dickinson point-counting method. *J. Sediment. Res.* **54**, 103–116 (1984).
29. Kahn, J. S. The analysis and distribution of the properties of packing in sand-size sediments: 1. On the measurement of packing in sandstones. *J. Geol.* **64**, 385–395 (1956).
30. Taylor, J. M. Pore-space reduction in sandstones. *AAPG Bull.* **34**, 701–716 (1950).
31. Poppe, L. J., Paskevich, V. F., Hathaway, J. C. & Blackwood, D. S. A laboratory manual for X-ray powder diffraction. *Open-File Report* <https://doi.org/10.3133/ofr0141> (2001).
32. SY/T 5163-2018. Analysis method for clay minerals and ordinary non-clay minerals in sedimentary rocks by the X-ray diffraction. (2018).
33. GB/T 14506.31-2019. Methods for chemical analysis of silicate rocks – Part 31: Determination of 12 components including silicon dioxide etc. – Lithium metaborate fusion-inductively coupled plasma atomic emission spectrometry. (2019).
34. GB/T 29171-2023. Rock capillary pressure measurement. (2023).
35. Çelik, M. Y. & Kaçmaz, A. U. The investigation of static and dynamic capillary by water absorption in porous building stones under normal and salty water conditions. *Environ. Earth Sci.* **75**, 307 (2016).
36. EN 1925: 1999. Natural stone test methods - Determination of water absorption coefficient by capillarity. (1999).
37. ASTM C97/C97M-25. Standard Test Methods for Absorption and Bulk Specific Gravity of Dimension Stone. (2025).
38. ASTM C170/C170M-24a. Standard Test Method for Compressive Strength of Dimension Stone. (2024).
39. ASTM D2845-05. Standard Test Method for Laboratory Determination of Pulse Velocities and Ultrasonic Elastic Constants of Rock. (2005).
40. Ulusay, R., Ersoy, H., Sünneci, M. O. & Karahan, M. The leeb (Equotip) hardness test for rock materials: An overview, assessments on the factors influencing test results, and prediction models based on a large database. *Bull. Eng. Geol. Environ.* **84**, 148 (2025).
41. EN 12370: 2020. Natural stone test methods -Determination of resistance to salt crystallisation. (2020).
42. Nesbitt, H. W. & Young, G. M. Early Proterozoic climates and plate motions inferred from major element chemistry of lutites. *Nature* **299**, 715–717 (1982).
43. Harnois, L. The CIW index: A new chemical index of weathering. *Sediment. Geol.* **55**, 319–322 (1988).
44. Pettijohn, F., Potter, P. & Siever, R. *Sand and Sandstones*. (Springer-Verlag, New York, 1972).
45. Ondrášik, M. & Kopecký, M. Rock pore structure as main reason of rock deterioration. *Stud. Geotechnica et. Mechanica* **36**, 79–88 (2014).
46. Bell, F. G. & Lindsay, P. The petrographic and geomechanical properties of some sandstones from the Newspaper Member of the Natal Group near Durban, South Africa. *Eng. Geol.* **53**, 57–81 (1999).
47. Howarth, D. F. & Rowlands, J. C. Quantitative assessment of rock texture and correlation with drillability and strength properties. *Rock. Mech. Rock. Engng* **20**, 57–85 (1987).
48. Mishra, D. A. & Basu, A. Estimation of uniaxial compressive strength of rock materials by index tests using regression analysis and fuzzy inference system. *Eng. Geol.* **160**, 54–68 (2013).
49. Shi, Z., Zhang, W. & Wang, Z. Correlation of physical and mechanical properties of Jurassic sandstone in Jining, Shandong province. *Arab J. Geosci.* **14**, 1254 (2021).
50. Wedekind, W., Poetzl, C., Doncel- López, R. & Siegesmund, M. Surface hardness testing for the evaluation of consolidation of porous low bound stones. in *Science and art: a future for stone* vol. I 491–499 (Paisley, 2016).
51. Dong, Z. et al. Evaluation of thermophysical and mechanical properties of sandstone due to high-temperature. *Materials* **15**, 8692 (2022).
52. Zhou, C., Huang, B. & Shu, X. Micromechanical model for predicting coefficient of thermal expansion of concrete. *J. Mater. Civ. Eng.* **25**, 1171–1180 (2013).
53. López-Doncel, R. et al. Thermal expansion on volcanic tuff rocks used as building stones: examples from Mexico. *Environ. Earth Sci.* **77**, 338 (2018).

54. Whitney, D. L. & Evans, B. W. Abbreviations for names of rock-forming minerals. *Am. Mineralogist* **95**, 185–187 (2010).

Acknowledgements

This work was jointly supported by the Science and Technology Major Special Program Project of Shanxi Province (No. 202201150501024), the Project of China-Portugal Belt and Road Joint Laboratory on Cultural Heritage Conservation Science (No. SDYY2301), the Project of Key Laboratory of Silicate Cultural Relics Conservation (Shanghai University), Ministry of Education (No. SCRC2024ZZ03YQ), and Xidun Education Foundation. The authors also thank Shanghai Technical Service Center of Science and Engineering Computing, Shanghai University for their support in this study.

Author contributions

X.G. acquired and interpreted most data in this study and wrote the manuscript. Y.Z. proposed the research framework, provided guidance for the experiments and revised the manuscript. R.H. performed the capillarity water absorption tests. R.Z. measured and analyzed the ultrasonic P-wave velocity. Y.C. provided guidance for this study. J.H. provided financial support and revised the manuscript. All authors read and approved the final manuscript.

Competing interests

The authors declare no competing interests.

Reprints and permissions information is available at <http://www.nature.com/reprints>

Publisher's note Springer Nature remains neutral with regard to jurisdictional claims in published maps and institutional affiliations.

Open Access This article is licensed under a Creative Commons Attribution-NonCommercial-NoDerivatives 4.0 International License, which permits any non-commercial use, sharing, distribution and reproduction in any medium or format, as long as you give appropriate credit to the original author(s) and the source, provide a link to the Creative Commons licence, and indicate if you modified the licensed material. You do not have permission under this licence to share adapted material derived from this article or parts of it. The images or other third party material in this article are included in the article's Creative Commons licence, unless indicated otherwise in a credit line to the material. If material is not included in the article's Creative Commons licence and your intended use is not permitted by statutory regulation or exceeds the permitted use, you will need to obtain permission directly from the copyright holder. To view a copy of this licence, visit <http://creativecommons.org/licenses/by-nc-nd/4.0/>.

© The Author(s) 2025

Additional information

Correspondence and requests for materials should be addressed to Yue Zhang or Jizhong Huang.